Journal Name

ARTICLE TYPE

Cite this: DOI: 10.1039/xxxxxxxxxx

Chemical control of dissolution-driven convection in partially miscible systems: theoretical classification

V. Loodts, L. Rongy and A. De Wit

Received Date
Accepted Date

DOI: 10.1039/xxxxxxxxxx

www.rsc.org/journalname

Dissolution-driven convection occurs in the host phase of a partially miscible system when a buoyantly unstable density stratification develops upon dissolution. Reactions can impact such convection by changing the composition and thus the density of the host phase. Here we study the influence of A+B$\rightarrow$ C reactions on such convective dissolution when A is the dissolving species and B a reactant initially present in the host phase. We perform a linear stability analysis of related reaction-diffusion density profiles to compare the growth rate of the instability in the reactive case to its non reactive counterpart when all species diffuse at the same rate. We classify the stabilizing or destabilizing influence of reactions on the buoyancy-driven convection in a parameter space spanned by the solutal Rayleigh numbers $R_{A,B,C}$ of chemical species A, B, C and by the ratio β of initial concentrations of the reactants. For $R_A > 0$, the non reactive dissolution of A in the host phase is buoyantly unstable. In that case, we show that reaction is enhancing convection provided C is sufficiently denser than B. Increasing the ratio β of initial reactant concentrations increases the effect of chemistry but does not significantly impact the stabilizing/destabilizing classification. When the non reactive case is buoyantly stable ($R_A < 0$), reactions can create in time an unstable density stratification and trigger convection if $R_C > R_B$. Our theoretical approach allows classifying previous results in a unifying picture and developing strategies for chemical control of convective dissolution.

1 Introduction

Dissolution-driven convection can occur in partially miscible systems when a phase dissolves into another one with a finite solubility. Even if the density stratification is initially buoyantly stable, a hydrodynamic instability can develop in the gravity field if the dissolution modifies the density of the host phase. This situation can happen in solutions separated by a semi-permeable membrane [1,2] or in biphasic systems, with the dissolving phase being for instance liquid [3,4], solid [5], or gaseous [6–13]. Dissolution-driven convection has recently gained much interest in the context of carbon dioxide (CO_2) capture or sequestration [14–16]. When CO_2 is injected in geological sites, it dissolves into a host liquid phase (oil or water), increasing thereby its density, which results in a buoyantly unstable density stratification. The contact zone between the denser CO_2-rich and the less dense bulk solution layers is then destabilized in the form of buoyancy-driven fingering [10–12,14–19]. It is of current interest to characterize this dissolution-driven convective instability as it contributes to the mechanism of CO_2 sequestration known as "solubility trapping" [15].

Université libre de Bruxelles (ULB), Faculté des Sciences, Nonlinear Physical Chemistry Unit, CP231, 1050 Brussels, Belgium.

In particular, the early-stage development of this instability has been characterized both theoretically and experimentally for porous media or Hele-Shaw cells with a focus on the critical time and wavenumber for the onset of convection [5,10–12,16,18–29]. Studies have reported the impact on these properties of boundary conditions [21,22,28], anisotropy of the permeability [16,23–25,28], geometry of the system [26], compressibility and interface movement [27], a geothermal gradient [28,29], and control parameters in laboratory experiments [5,10–12,19]. However, an important aspect that has been less investigated is the impact of chemical reactions on such instabilities. This is important as geochemical reactions may occur between dissolved CO_2 and minerals in geological storage sites [30–34].

It is known that chemical reactions can affect the density of the solution and thus impact the development of buoyancy-driven instabilities in miscible [35–37] and immiscible systems [38]. Reactions can similarly affect the early-stage development of dissolution-driven convection [3,13,31–34]. A reaction between the dissolving species and a solid delays the onset of convection as the reaction consumes the dissolving species at the origin of the instability [31–34]. However, as the solid reactant is static, the dissolving species is then the only one contributing to the dynamics in the

fluid phase. By contrast, it has been shown in miscible systems that when all species contribute to hydrodynamics, different behaviors can be observed[35,39,40].

Recently, we have shown that chemical reactions with a dissolved reactant can either stabilize[3,13] or destabilize[13] dissolution-driven convection compared to the non reactive case. In particular, we have shown an experimental example of a reaction that accelerates the onset of convection after dissolution of CO_2 in an aqueous host phase. The dissolving CO_2 reacts with a base (sodium hydroxide, NaOH) present in the host phase, leading to density profiles even more unstable with regard to convection than the non reactive profile. For the case of an ester on top of water, its dissolution can on the contrary be slowed down by a reaction[3]. We have shown theoretically that the relative contributions of the dissolved reactant and product to the density can control the effects of reactions on dissolution-driven convection[13]. However, the system is also characterized by other parameters, such as the contribution of the dissolving species to the density or the ratio between the initial concentration of the reactants. There is thus a need to assess the impact of these parameters on the possibility of a reaction to control the convective dissolution.

In this context, the objective of this study is to propose a general framework to classify the effects of A+B $\rightarrow$ C chemical reactions between the dissolving species A and a dissolved reactant B on the early-stage development of dissolution-driven convection. To do so, we consider both cases where the dissolving species increases or decreases the density in the host phase. We also analyze the impact on convection of the ratio of initial reactant concentrations. This generalized classification highlights the link between previous disparate studies and paves the way for predictions in new experimental systems. More specifically, we couple the incompressible Darcy's equations for the velocity of the fluid in a porous medium to two-dimensional reaction-diffusion-convection (RDC) equations for the concentration fields through a linear state equation for the density of the fluid. We suppose that all diffusion coefficients are equal to avoid any double diffusive instabilities. We first classify the generic reaction-diffusion (RD) density profiles as a function of their properties (monotonic or non-monotonic), which impacts the development of dissolution-driven convection. To quantify the effect of the reaction on the instability, we then perform a linear stability analysis.

This article is structured as follows: in section 2 we describe the physical system and the model. We classify the RD density profiles in section 3. In section 4, we describe the method of linear stability analysis and use it to characterize the early-stage development of the instability for different areas of the parameter space. Finally, in section 5, we show how our classification encompasses previous studies and we discuss the implications of our results for possible applications, in particular CO_2 sequestration.

2 Description of the physical model

Let us consider a pure phase A, called here the dissolving phase or species, which dissolves into a host solution containing a reactant B at an initial concentration B_0[3,13]. The two phases are in contact

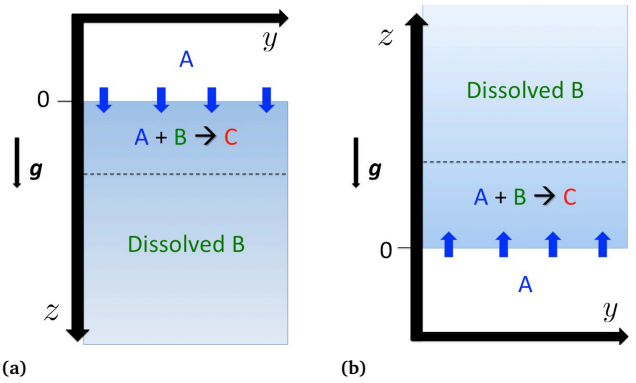

Fig. 1 Two-dimensional model system. The dashed line represents the boundary layer of A dissolving into the host phase. Case (a): the host phase is below the dissolving phase; case (b): the host phase is above the dissolving phase.

along a horizontal interface and the initial condition is buoyantly stable with the less dense phase lying on the top. Figure 1a illustrates the case where the denser host phase is located below the less dense dissolving phase while the opposite case (less dense host phase on the top) is shown in Fig.1b.

We assume a local equilibrium at the interface located at $z = 0$ so that the concentration of A at the interface is always equal to its solubility A_0 in the host phase, which may depend on experimental parameters (temperature, salinity, pressure, ...)[19] and is not limited by diffusion. We assume that the volume of the host phase does not change significantly upon dissolution of A and do not consider any thermal[29,41] or dispersion effects[42].

We further assume that the interface is only permeable to A but impermeable to B and C, i. e. B and C can not dissolve into phase A. In this situation, we can focus on the dynamics in the host phase only, which is considered infinite in the horizontal direction y and semi-infinite in the vertical direction z from the interface located at $z = 0$ to the bulk of the reactive host phase at $z \rightarrow \infty$. A and B react in the host phase according to the reaction A+B $\rightarrow$ C with a kinetic constant q.

To describe the dynamics in the host phase, we choose Darcy's equations as flow equations for the incompressible velocity field $\boldsymbol{u} = (u, v)$ because it describes flow dynamics in porous media like geological sites for CO_2 storage[14] and thin Hele-Shaw cells[43] used in laboratory experiments. The incompressible Darcy's equations read:

$$\boldsymbol{\nabla} p = -\frac{\mu}{\kappa}\boldsymbol{u} + \rho \mathbf{g}, \tag{1a}$$

$$\boldsymbol{\nabla} \cdot \boldsymbol{u} = 0, \tag{1b}$$

where p is the pressure and ρ is the density of the host solution. The dynamic viscosity μ, permeability κ and norm of the gravity field $g = \|\boldsymbol{g}\|$ are assumed constant.

The RDC equations governing the evolution of the concentra-

tion fields A, B and C read:

$$\frac{\partial A}{\partial t}+(\boldsymbol{u}\cdot\boldsymbol{\nabla})A = D_A\nabla^2 A - qAB, \quad (2a)$$

$$\frac{\partial B}{\partial t}+(\boldsymbol{u}\cdot\boldsymbol{\nabla})B = D_B\nabla^2 B - qAB, \quad (2b)$$

$$\frac{\partial C}{\partial t}+(\boldsymbol{u}\cdot\boldsymbol{\nabla})C = D_C\nabla^2 C + qAB. \quad (2c)$$

To avoid any double diffusive instabilities, we assume that the molecular diffusion coefficients D_j are constant and equal ($D = D_A = D_B = D_C$). The following linear state equation for ρ [25] couples Eqs.(1) and Eqs.(2):

$$\rho = \rho_0(1+\alpha_A A+\alpha_B B+\alpha_C C), \quad (3)$$

where ρ_0 is the density of the solvent of the lower phase, $\alpha_j = \frac{1}{\rho_0}\frac{\partial \rho}{\partial j}$ is the solutal expansion coefficient of species j of concentration j.

To obtain dimensionless equations, we use the characteristic RD scales [13,39,40]: length $l_c = \sqrt{Dt_c}$, velocity $u_c = \sqrt{D/t_c}$ with the reactive time scale t_c defined as

$$t_c = \frac{1}{qA_0}. \quad (4)$$

For the case illustrated in Fig.1a, where the gravity field and the z axis have the same direction ($\boldsymbol{g} = g\,\mathbf{1}_z$ with $\mathbf{1}_z$ the unit vector along z), we define

$$\tilde{A} = A/A_0, \quad \tilde{B} = B/A_0, \quad \tilde{C} = C/A_0, \quad (5a)$$

$$\tilde{\boldsymbol{z}} = \boldsymbol{z}/l_c, \quad \tilde{t} = t/t_c, \quad \tilde{\boldsymbol{u}} = \boldsymbol{u}/u_c, \quad (5b)$$

$$\tilde{p} = \frac{p-p_a-\rho_0 gz}{p_c}, \quad \tilde{\rho} = \frac{(\rho-\rho_0)g\kappa l_c}{\mu D}. \quad (5c)$$

The ambient pressure p_a, the hydrostatic pressure $\rho_0 gz$ and the pressure scale $p_c = \mu D/\kappa$ have been used to define a dimensionless dynamic pressure.

Substituting the nondimensional quantities (5) in Eqs.(1)-(3) and dropping tildes for convenience leads to the dimensionless model

$$\boldsymbol{\nabla} p = -\boldsymbol{u} + (R_A A + R_B B + R_C C)\,\mathbf{1}_z, \quad (6a)$$

$$\boldsymbol{\nabla}\cdot\boldsymbol{u} = 0, \quad (6b)$$

$$\frac{\partial A}{\partial t}+(\boldsymbol{u}\cdot\boldsymbol{\nabla})A = \nabla^2 A - AB, \quad (6c)$$

$$\frac{\partial B}{\partial t}+(\boldsymbol{u}\cdot\boldsymbol{\nabla})B = \nabla^2 B - AB, \quad (6d)$$

$$\frac{\partial C}{\partial t}+(\boldsymbol{u}\cdot\boldsymbol{\nabla})C = \nabla^2 C + AB, \quad (6e)$$

where R_j is the solutal Rayleigh number of species j expressed for the case illustrated in Fig.1a as

$$R_j = \frac{\alpha_j A_0\,\kappa l_c}{\nu D}\,g \quad (7)$$

with $\nu = \mu/\rho_0$ the kinematic viscosity of the solvent. In the rest of this study, we will focus on the description of the case shown in Fig.1a. It is, however, straightforward to extend the conclusions of our study to the case shown in Fig.1b ($\boldsymbol{g} = -g\,\mathbf{1}_z$) by replacing g by $-g$ in Eq.(7). Note that the Rayleigh number R_A is positive in case (1a) if $\alpha_A > 0$, i.e. A dissolves from the top of the host phase and increases the density of the solution. In case (1b) where A dissolves from the bottom of the host phase, $R_A > 0$ if $\alpha_A < 0$, i.e. A decreases the density of the solution. In both cases without reaction, $R_A > 0$ corresponds then to the development of a buoyantly unstable density stratification upon dissolution of A in the host phase while $R_A \leq 0$ corresponds to the stable case.

The dimensionless density of the solution can be reconstructed from the concentration fields as

$$\rho = R_A A + R_B B + R_C C. \quad (8)$$

We note that in Eq.(8), R_j quantifies the contribution of species j to the density of the solution. Introducing in Eqs.(6) the stream function Ψ with $u = -\Psi_z$ and $v = \Psi_y$, which satisfies Eq.(6b), and using the notation $\partial_x f = \frac{\partial f}{\partial x}$ for the derivative of a function f relative to a variable x yields:

$$\nabla^2\Psi = R_A\partial_y A + R_B\partial_y B + R_C\partial_y C, \quad (9a)$$

$$\partial_t A - \partial_z\Psi\,\partial_y A + \partial_y\Psi\,\partial_z A = \nabla^2 A - AB, \quad (9b)$$

$$\partial_t B - \partial_z\Psi\,\partial_y B + \partial_y\Psi\,\partial_z B = \nabla^2 B - AB, \quad (9c)$$

$$\partial_t C - \partial_z\Psi\,\partial_y C + \partial_y\Psi\,\partial_z C = \nabla^2 C + AB. \quad (9d)$$

with $\nabla^2 = \frac{\partial^2}{\partial y^2} + \frac{\partial^2}{\partial z^2}$. The initial conditions at $t = 0$ and $\forall y$ are

$$\Psi(z) = 0 \quad \forall z, \quad (10a)$$

$$A(z=0) = 1; \quad A(z>0) = 0, \quad (10b)$$

$$B(z) = \beta = B_0/A_0 \quad \forall z, \quad (10c)$$

$$C(z) = 0 \quad \forall z. \quad (10d)$$

The boundary conditions $\forall y, t$ are

$$\Psi(z=0) = 0; \quad \Psi(z\to\infty) = 0, \quad (11a)$$

$$A(z=0) = 1; \quad A(z\to\infty) = 0, \quad (11b)$$

$$\partial_z B(z=0) = 0; \quad B(z\to\infty) = \beta, \quad (11c)$$

$$\partial_z C(z=0) = 0; \quad C(z\to\infty) = 0. \quad (11d)$$

The addition of Eqs.(9c) and (9d) with the initial conditions (10c)-(10d) and boundary conditions (11c)-(11d) shows that $(B+C)$ remains constant over time and equal to its initial value β. Therefore, the concentration field C can be reconstructed from B with

$$C = \beta - B, \quad \forall y, z, t. \quad (12)$$

By inserting Eq.(12) in Eq.(9a), our final model is function of A

and B only and reads:

$$\nabla^2\Psi = R_A\partial_y A - (R_C - R_B)\partial_y B, \quad (13a)$$

$$\partial_t A - \partial_z\Psi\,\partial_y A + \partial_y\Psi\,\partial_z A = \nabla^2 A - AB, \quad (13b)$$

$$\partial_t B - \partial_z\Psi\,\partial_y B + \partial_y\Psi\,\partial_z B = \nabla^2 B - AB. \quad (13c)$$

Further, we also simplify the expression for the density profile in the host phase by inserting Eq.(12) in Eq.(8):

$$\rho = R_A A - (R_C - R_B)B + R_C\beta. \quad (14)$$

The parameters of the model are the Rayleigh number R_A, the difference $R_C - R_B$ between the Rayleigh numbers of C and B, and the initial concentration β of reactant. Let us classify the RD density profiles reconstructed from the RD concentration profiles with Eq.(14).

3 Classification of Reaction-Diffusion density profiles

It is crucial to analyze the RD density profiles to qualitatively understand the development of the buoyancy-driven instability. In the non reactive case, the only species contributing to the density profile is A. Its concentration profile is solution of Fick's law $2\eta A' + A'' = 0$ with the notations $f' = \frac{df}{d\eta}$, $f'' = \frac{d^2 f}{d\eta^2}$ and η the self-similar variable $\eta = \frac{z}{2\sqrt{t}}$, the initial conditions (10b) and the boundary conditions (11b), i. e. $A = 1 - \mathrm{erf}(\eta)$. The related non reactive density profile is thus

$$\rho(\eta) = R_A A(\eta) = R_A[1 - \mathrm{erf}(\eta)]. \quad (15)$$

Figure 2a shows that the non reactive concentration profile is monotonically decreasing as A enters into the solution from the interface and then diffuses to the bulk of the host phase. When $R_A > 0$, in case 1a, A increases the density of the solution upon dissolution, which leads to a denser zone rich in A above the less dense host bulk solvent [16–19,44]. In case 1b, A decreases the density of the solution upon dissolution so that a less dense zone rich in A forms below the denser host bulk solvent. The density stratification that develops over time is then buoyantly unstable in both non reactive cases. On the contrary, if $R_A \leq 0$, A decreases (or does not affect) in case 1a and increases (or does not affect) in case 1b the density of the solution upon dissolution. In both non reactive cases, the density stratification that develops over time is then buoyantly stable.

In the reactive case, all three contributions of A, B and C have to be taken into account to reconstruct the density profile. The RD concentration profiles of A and B are obtained by solving Eqs.(9b)-(9c) without flow, withe the initial conditions (10b)-(10c) and the boundary conditions (11b)-(11c):

$$\partial_t A = \nabla^2 A - AB, \quad (16a)$$

$$\partial_t B = \nabla^2 B - AB. \quad (16b)$$

Let us recall that the concentration profile of C can be reconstructed from B with Eq.(12) with the initial conditions (10d) and the boundary conditions (11d). Note that the solution of Eqs.(16) depends on β only, which appears in the initial condition (10c).

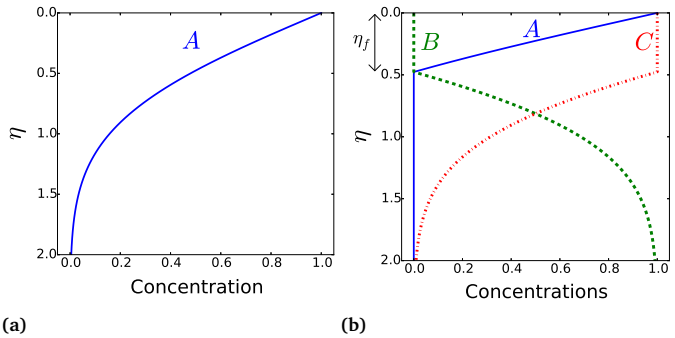

Fig. 2 (a) Non reactive concentration profile of A; (b) Asymptotic RD concentration profiles (18) for $\beta = 1$.

3.1 A+B → C reaction fronts in partially miscible systems

Because Eqs.(16) are non linear, they do not admit general analytical solutions. Following the reasoning of previous works [39,45,46], we can, however, compute analytical asymptotic solutions. At large times, the consumption of the reactants is no more limited by the reaction but rather limited by the rate at which the species diffuse to the reaction zone. In this limit, the reaction is localized at a reaction front where A and B are immediately and entirely consumed, while there is no reaction anywhere else (Fig.2b). This reaction front moves on a diffusive time scale and is thus located at $z_f = 2\eta_f\sqrt{t}$ with $\eta_f > 0$. Outside the reaction front, the concentration fields j are solutions of diffusive equations $2\eta j' + j''$ with the boundary conditions

$$\eta = 0: \quad A = 1, \quad B = 0, \quad (17a)$$

$$\eta = \eta_f: \quad A = 0, \quad B = 0, \quad (17b)$$

$$\eta \to \infty: \quad A = 0, \quad B = \beta. \quad (17c)$$

The asymptotic concentration fields between the interface and the reaction front ($0 \leq \eta \leq \eta_f$) denoted by "U" as "Upper" and those between the reaction front and the bulk of the solution ($\eta_f < \eta < \infty$) denoted by "L" as "Lower" are:

$$A^U = 1 - \frac{\mathrm{erf}(\eta)}{\mathrm{erf}(\eta_f)}, \quad A^L = 0, \quad (18a)$$

$$B^U = 0, \quad B^L = \beta\left(1 - \frac{\mathrm{erfc}(\eta)}{\mathrm{erfc}(\eta_f)}\right). \quad (18b)$$

To compute these concentration profiles (18), we need to calculate η_f by equalizing the fluxes of A and B at the reaction front, i.e. $-\partial_\eta A^U(\eta_f) = \partial_\eta B^L(\eta_f)$, which yields

$$\mathrm{erf}(\eta_f) = \frac{1}{1+\beta}. \quad (19)$$

η_f is computed from Eq.(19) with a Newton-Raphson iteration [47]. In particular, for $\beta = 1$, η_f is equal to $\mathrm{erfinv}(0.5) \approx 0.48$. Figure

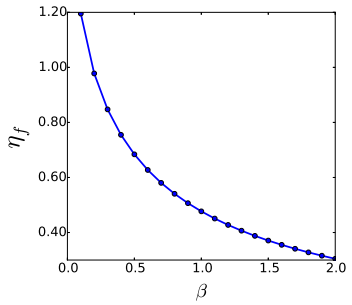

Fig. 3 Position of the reaction front η_f as a function of the initial concentration β of reactant.

3 shows that, when β increases, the reaction front η_f becomes closer to the interface in self-similar coordinates, i.e. moves slower towards the bulk of the solution.

Figure 2b shows the asymptotic RD concentration profiles (18). The dissolving species A enters the solution from the interface where its concentration is maximum and is then consumed by the reaction. The reaction front advances in time away from the interface towards the bulk of the solution ($z_f = 2\eta_f\sqrt{t}$ with $\eta_f > 0$). Between the interface and the reaction front, B has been totally consumed to produce C. The concentration of B increases from 0 at $\eta = \eta_f$ to its initial value β in the bulk of the solution. C is present mainly between the interface and the reaction front but also extends to the bulk of the solution by diffusion. We note that, in the limit of instantaneous reactions, the length scale $l_c = \sqrt{D_A t_c}$ becomes small (see Eq.(4)), so that the zone between the interface and the reaction front can be neglected and only the region between the reaction front and the bulk solution be considered[9]. In summary, the system is divided into three zones: between the interface and the reaction front ($0 \leq \eta < \eta_f$) where only A and C are present, between the reaction front and the bulk solution ($\eta_f < \eta < \infty$) where B and C are the only chemical species in presence, and the bulk solution ($\eta \to \infty$) where only B remains.

3.2 Asymptotic density profiles

We obtain the asymptotic RD density profiles by inserting Eqs.(18) in Eq.(14):

$$\rho^U = R_A\left(1 - \frac{\mathrm{erf}(\eta)}{\mathrm{erf}(\eta_f)}\right) + R_C\beta, \tag{20a}$$

$$\rho^L = (R_C - R_B)\beta\left(\frac{\mathrm{erfc}(\eta)}{\mathrm{erfc}(\eta_f)} - 1\right) + R_C\beta. \tag{20b}$$

Extrema in the density profile have been shown to affect the behavior of chemically-driven buoyancy convection, depending on the relative contribution of each species to the density[13,39,40,46]. We thus look for the presence of extrema created by the reaction in the density profile ρ (20), by analyzing for what value of parameters its derivative ρ_η changes sign at a given location. The

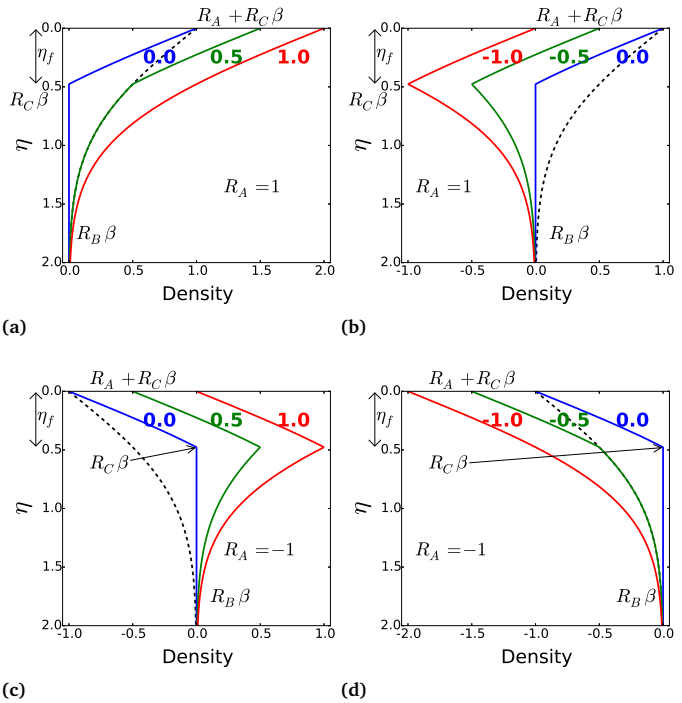

Fig. 4 Asymptotic RD density profiles (20) with $\beta = 1$, $R_B = 0$ and values of R_C indicated on the graphs. The non-reactive (NR) density profile is plotted as a dashed curve. (a) $R_A = 1$ and $R_C - R_B \geq 0$; (b) $R_A = 1$ and $R_C - R_B \leq 0$; (c) $R_A = -1$ and $R_C - R_B \geq 0$; (d) $R_A = -1$ and $R_C - R_B \leq 0$.

derivatives of ρ^U and ρ^L relative to η are

$$\rho^U_\eta = -\frac{2}{\sqrt{\pi}}\frac{R_A}{\mathrm{erf}(\eta_f)}e^{-\eta^2}, \tag{21a}$$

$$\rho^L_\eta = -\frac{2}{\sqrt{\pi}}\frac{(R_C - R_B)\beta}{\mathrm{erfc}(\eta_f)}e^{-\eta^2}. \tag{21b}$$

The sign of ρ^U_η depends on R_A only and the sign of ρ^L_η depends on $R_C - R_B$ only. If R_A and $R_C - R_B$ have the same sign, ρ^U_η and ρ^L_η are both increasing or both decreasing, so that the global density profile is monotonic. Therefore, an extremum can appear at the reaction front only if R_A and $R_C - R_B$ have opposite signs.

Figure 4 shows the reactive density profiles (20) plotted for different R_A and $R_C - R_B$. The non reactive density profile (15) is also plotted as a dashed black curve for comparison. The upper figures 4a and 4b illustrate the case $R_A > 0$ when the non reactive density profile is already unstable. If $R_C - R_B \geq 0$ as in Fig. 4a, the density profile is monotonically decreasing along η like its non reactive counterpart. By contrast, if $R_C - R_B < 0$, the density profile has a minimum created by the reaction (see Fig.4b). Indeed, the upper part of the density profile (above the reaction front) is decreasing due to the contribution of A to density. At the reaction front, only C contributes to the density with a contribution equal to $R_C\beta$. Far into the bulk solution, only B contributes to the density, and the density of the solution comes back to its initial value $R_B\beta$. As R_C is smaller than R_B, a minimum appears at the reaction front. That minimum affects the stability of the density profile because locally less dense fluid lies on top of denser

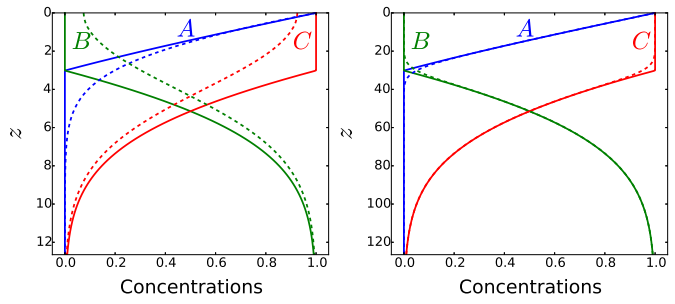

(a) (b)

Fig. 5 Asymptotic concentration profiles (18) (plain line) and numerical concentration profiles (dashed line) for $\beta = 1$, at times (a) 10 and (b) 1000.

fluid[3,13].

The lower figures 4c and 4d illustrate the case $R_A \leq 0$ when the non reactive density profile is monotonically increasing along η and stable. If $R_C - R_B \leq 0$ like R_A, the density profile remains stable (see Fig.4d). In the opposite case, if $R_C - R_B > 0$, a maximum is created by the reaction (see Fig.4c). Similarly to the case $R_A > 0$ and $R_C - R_B < 0$, this can be explained by the different contributions of the species to density. This maximum affects the stability of the system as locally denser fluid lies on top of less dense fluid. We suspect that this maximum destabilizes the system with regard to non reactive buoyancy-driven convection.

3.3 Numerical density profiles

As the analytical asymptotic density profiles are only valid for fast reactions or long times, we check that the classification discussed in subsection 3.2 is also valid for density profiles computed numerically at different times. Equations (16) are solved numerically using a Crank-Nicolson method[47]. We approximate a semi-infinite system by taking a system long enough such that the RD concentration profiles are not affected by the lower boundary.

Figure 5 shows that the numerical concentration profiles converge over time to the analytically predicted concentration profiles. We will nevertheless use the numerical concentration profiles, valid for all times, to perform the linear stability analysis used to assess the stability of the RD profiles (see Section 4). However, we have checked that the classification discussed in subsection 3.2 still holds at short times as the profiles are qualitatively similar.

4 Characterization of the instability

In this section, a linear stability analysis (LSA) is used to compare the stability of the density profiles to their non reactive counterpart. We recall that the parameters defining the problem are β, R_A and $R_C - R_B$.

4.1 Method of linear stability analysis

There exist several methods of LSA with different constraints or drawbacks linked to the starting assumptions and that give different results depending on how the perturbation growth is defined and measured[20,48,49]. We note, however, that all these methods give a time for the linear onset of convection on the same order of magnitude than experimental results[5]. Here we make the quasi-steady state approximation (QSSA) that the perturbations vary at a much faster pace than the base state solutions so that these solutions can be considered frozen at a given time t_f[13,50]. We add normal form perturbations to the base state profiles such as

$$\begin{aligned}(A,B,C,\Psi)(y,z,t_f+\Delta t) &= (A^s,B^s,C^s,0)(z,t_f) \\ &+ e^{\sigma(t_f+\Delta t)+iky}(a,b,c,ik\psi)(z)\end{aligned} \tag{22}$$

with $i^2 = -1$, k the wavenumber and σ the growth rate of the perturbation.

We substitute (22) in Eqs.(13), and neglect non linear perturbative terms, which gives

$$\partial_{zz}\psi - k^2\psi = k^2(R_A a - (R_C - R_B)b), \tag{23a}$$

$$\sigma a - \partial_z A^s \psi = \partial_{zz}a - k^2 a - B^s a - A^s b, \tag{23b}$$

$$\sigma b - \partial_z B^s \psi = \partial_{zz}b - k^2 b - B^s a - A^s b, \tag{23c}$$

with the notation $\partial_{xx} f = \frac{\partial^2 f}{\partial x^2}$. Equations (23) are solved numerically on a discrete set of points with the derivatives approximated using finite differences to allow the system to be expressed in matrix form and yield the eigenvalue problem

$$\underline{\underline{J}} \cdot \underline{s} = \sigma \underline{s}, \tag{24}$$

A dispersion curve representing the growth rate of the perturbation σ as a function of its wavenumber k is obtained by plotting the largest real part of eigenvalue σ for a given k. We have performed convergence tests to find the optimal discretization for space and time. Typical values for the length of the numerical domain and the mesh size to achieve an accuracy of 1.0% in the computation of the maximum growth rates are 400 and 0.25, respectively. For this domain length of 400 or larger, the assumption of semi-infinite domain is thus valid as the profile is not affected by the lower boundary.

From the dispersion curves obtained at different frozen times, we extract the maximum growth rate σ_m corresponding to the most unstable wavenumber k_m. Figure 6a illustrates the typical variation of σ_m and k_m with time for $R_A > 0$. The system is initially stable with regard to buoyancy-driven convection as σ_m is negative. Some time is indeed needed to build a denser fluid layer that is sufficiently extended to trigger the instability. σ_m increases over time, so that after some time, it changes sign and becomes positive. This means that the system becomes unstable with regard to convection. σ_m continues to increase with time up to a maximum value and then decreases. This decrease is related to a weakening of the unstable density gradient by diffusion as time goes by. The wavenumber k_m associated to the maximum growth rate can also vary non monotonically as a function of time as shown in Fig. 6b.

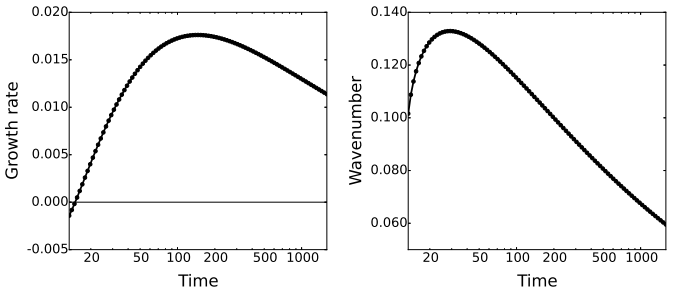

Fig. 6 (a) Maximum growth rate σ_m and (b) most unstable wavenumber k_m of the dispersion curves as a function of time with $\beta = 1$, $R_A = 1$ and $R_C - R_B = 1$.

4.2 Definition of the characteristics of the instability

Most previous papers devoted to a LSA of a transient growing boundary layer have characterized the instability by the onset time t^0 at which $\sigma_m = 0$, beyond which the system thus becomes unstable, and by the related onset wavenumber k_m^0 [20,48]. At this time, however, as the growth rate is by definition equal to zero, we have no information on the growth of the perturbation. Instead, to avoid any dependence on the initial conditions, we compute a characteristic growth rate σ^* of the instability quantifying the rate at which perturbations grow once the system is unstable and still in the linear regime. Following Trevelyan et al. [51], the characteristic growth rate σ_m^* is defined as the maximum growth rate at t^* for which $\sigma_m^* t^* = 1$, such that the amplification factor $\exp(\sigma_m^* t^*)$ of the perturbation at t^* is of order unity. We also compute the characteristic wavelength $\lambda_m^* = 2\pi/k_m^*$, where k_m^* is the wavenumber corresponding to σ_m^* at t^* and is thus the fastest developing mode at t^*. We aim to compare these characteristic values in the reactive case to those in the non reactive (NR) case. Adapting the parameterless characteristic values for the NR case [19] in our scalings gives for $R_A > 0$, $t_{NR}^* = 252 R_A^{-2}$, $\sigma_{NR}^* = 3.96 \times 10^{-3} R_A^2$, $k_{NR}^* = 6.19 \times 10^{-2} R_A$, $\lambda^*{}_{NR} = 101.5/R_A$. σ_{NR}^* is in agreement with experimental [5] and numerical [44,52] values reported in the literature for the growth of the dissolution-driven perturbation in the linear regime. For $R_A \leq 0$, the non reactive density profile is always stable as σ_m is always negative.

4.3 Effects of reactions on the characteristics of the instability in the case $R_A > 0$

Using the linear stability analysis described above, we compare the characteristics of the instability - growth rate σ_m^* and wavelength λ_m^* - in the reactive case to their counterparts in the non reactive case. We first analyse the case $R_A > 0$ when a buoyantly unstable density stratification develops upon dissolution of A. Figure 7a shows that when $R_A > 0$, σ_m^* increases with $R_C - R_B$, corresponding to replacing reactant B with an increasingly denser product C. For small values of $R_C - R_B$, σ_m^* is smaller than the non reactive growth rate σ_{NR}^*. We can then define Δ_R as the critical value of $R_C - R_B$ needed for σ_m^* to be larger than σ_{NR}^*. As a consequence of this definition, if $R_C - R_B < \Delta_R$ (regions I-II), $\sigma_m^* < \sigma_{NR}^*$: the perturbation grows slower in the reactive system than in the absence of reaction, and the reaction stabilizes the system with regard to convection. On the contrary, if $R_C - R_B > \Delta_R$ (region III), $\sigma_m^* > \sigma_{NR}^*$: the reaction accelerates the development of the perturbation. We find that Δ_R slightly changes with β (Fig.7).

In zone I ($R_C - R_B < 0$), the RD density profiles have a minimum located at the reaction front η_f where locally less dense fluid lies on top of denser fluid (stable situation). When $R_C - R_B$ increases, the weight of the fluid layer above the reaction front remains the same compared to the minimum of density $R_C\beta$, but the density difference between this minimum and the density of the bulk solution $R_B\beta$ decreases (see Fig.4b). The decrease of this density difference with $R_C - R_B$ explains the increase of the characteristic growth rate. It is thus the zone below the minimum which acts as a stabilizing barrier and slows down the development of convection.

In zone II ($0 \leq R_C - R_B < \Delta_R$), by contrast, the RD density profiles are monotonic (see Fig.4a). We can easily understand the stabilizing effect of reactions in zone II when $R_B = R_C$: the consumption of B is exactly compensated by the production of C in terms of density, but the species A, which increases the density, is consumed by the chemical reaction. Hence, the global effect of reaction is to weaken the density stratification at the origin of the instability. Δ_R can thus be seen as the additional contribution to density that C must have with respect to B to compensate for the consumption of A.

In zone III ($R_C - R_B > \Delta_R$), C is dense enough to more than compensate for the loss of A by reaction. The perturbation grows faster than in the non reactive case ($\sigma_m^* > \sigma_{NR}^*$), and the reactive system is more unstable with regard to buoyancy-driven convection than its non reactive counterpart.

In addition, Fig.7a shows that increasing the initial concentration β of reactant amplifies the effect of the reaction (stabilizing or destabilizing). If the reaction slows down the growth of the perturbation (zones I-II), the growth rate decreases with β. In zone I, the density difference between the minimum of density and the bulk solution, $(R_C - R_B)\beta$, indeed increases with β. We can explain the stabilizing effect observed in zone II by the increase with β of the consumption of A, which decreases the weight of the denser fluid layer. If the reactive system is more unstable than the non reactive one (zone III), the growth rate increases with β because the production of C, which increases the weight of the denser fluid layer, increases with β.

Figure 7b shows that, for all values of $R_C - R_B$, the wavelength λ_m^* is smaller in the reactive system than in the non reactive one. In zone I, the wavelength does not vary significantly with $R_C - R_B$, while it decreases in zone III. λ_m^* decreases with β everywhere except in zone II. The reason why in this zone II, λ_m^* has a maximum and the effect of β is reversed remains unclear.

As Δ_R plays a major role in the classification of the effects of reactions, we detail below its variation with R_A and β. Figure 8a shows that Δ_R linearly increases with $R_A > 0$ as $\Delta_R = 0.32 R_A + 0.00$. We recall that Δ_R represents the excess contribution to density that C must have with respect to B to compensate for the consumption of A. Since R_A represents the contribution of A to the density of the solution, Δ_R increases when A contributes more to

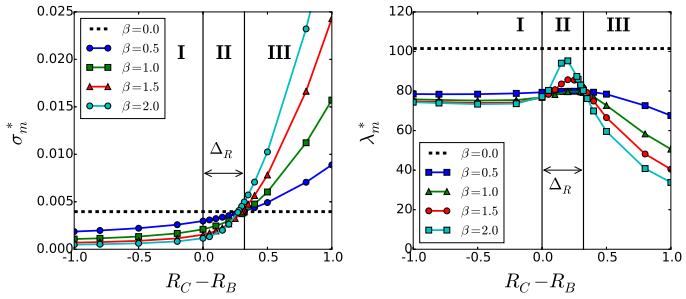

Fig. 7 Characteristic (a) growth rate and (b) wavelength of the instability as a function of $R_C - R_B$ with $R_A = 1$, and various β. The non reactive values are given by the dashed black line ($\beta = 0.0$). The critical value Δ_R varies slightly as a function of β (see Fig.8b) and is shown in the graph for $\beta = 1$.

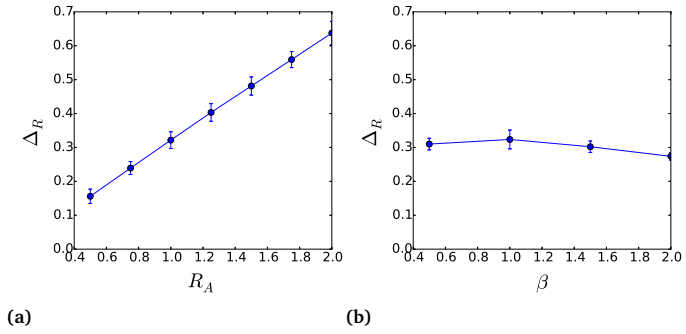

Fig. 8 (a) Critical value Δ_R as a function of R_A for $\beta = 1$; (b) critical value Δ_R as a function of β for $R_A = 1$.

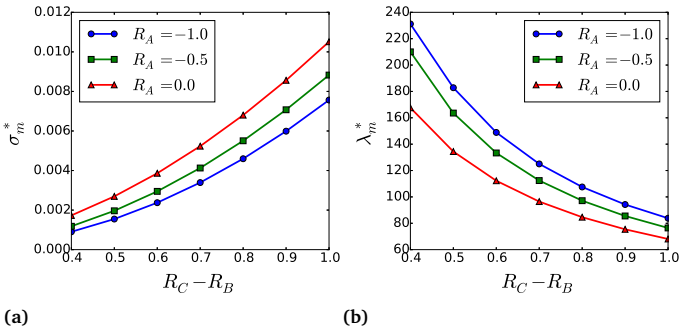

Fig. 9 Characteristic (a) growth rate and (b) wavelength of the instability as a function of $R_C - R_B$ with $\beta = 1$, and different negative R_A.

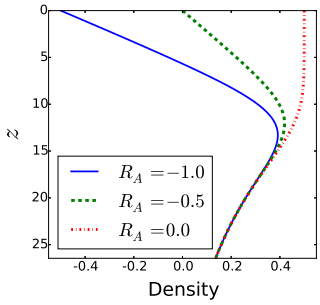

Fig. 10 Numerical density profiles for $t = t^*_{NR}$, $\beta = 1$, $R_B = 0.0$ and $R_C = 0.1$ and different $R_A \leq 0$.

the density, i.e., the product C must be denser to compensate for the consumption of the increasingly denser species A.

Figure 8b shows that the variation of Δ_R with β is much smaller than its variation with R_A. We have represented the error on Δ_R computed from the propagation of error on σ_m in Fig.8b to show that the non monotonic variation of Δ_R with β is within the error and thus possibly non significant for the concentration range tested here. However, from $\beta = 1.5$ to $\beta = 2.0$, the decrease of Δ_R is slightly larger than the error. When β increases, the reaction becomes stronger: the consumption of A increases, which tends to decrease the extent of the denser fluid layer at the origin of the instability (see Fig.3). In addition to the weight of the denser layer, the local gradient probably influences the stability of the density profile, which renders physical interpretation intricate.

4.4 Effects of reactions on the characteristics of the instability in the case $R_A \leq 0$

The non reactive case for $R_A \leq 0$ is stable for all times, which means that all modes have a negative growth rate. We recall that this corresponds here to the buoyantly stable dissolution downwards (Fig.(1a)) of a solute A decreasing density ($\alpha_A \leq 0$) or upwards (Fig.(1b)) of a solute increasing density ($\alpha_A \geq 0$). We will thus not compare the reactive case to the non reactive case but rather discuss when the reaction *creates* buoyancy-driven convection, and in that case what parameters increase the growth rate of the perturbation.

Figure 9a shows that when $R_A \leq 0$, the perturbation is characterized by a positive growth rate only when $R_C - R_B > 0$ (zone

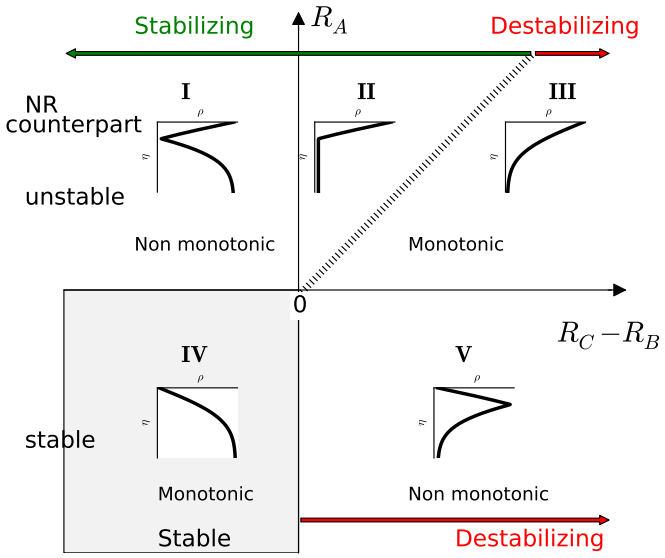

Fig. 11 Classification of the density profiles as a function of $R_C - R_B$ and R_A. Zone I: non monotonic stabilizing, zone II: monotonic stabilizing, zone III: monotonic destabilizing, zone IV: monotonic stable, zone V: non monotonic destabilizing. The dashed diagonal is the line $R_A = (R_C - R_B)/0.32$ which separates zones II and III (see Fig.8a).

V in Fig.11), i.e. when a maximum appears in the density profile thanks to the reaction (see Fig.4c). Note that we have not represented characteristic values corresponding to small $R_C - R_B$ in Fig.9 because the numerical system is finite and the diffusive profile reaches the boundary of the system before the characteristic time. A semi-infinite system, however, should be unstable even for small $R_C - R_B > 0$ at arbitrarily large times. The initially stable system is destabilized with regard to convection because the reaction creates a non monotonic density profile with a maximum where locally denser fluid lies on top of a less dense one. σ_m^* increases with $R_C - R_B$ because the amplitude of the maximum compared to the bulk solution increases with $R_C - R_B$ (see Fig.4c). Figure 10 shows that for $R_A = 0$, the denser area extends from the interface down to the reaction front while it becomes more localized near the reaction front when R_A decreases. In addition, C must be denser to compensate for the larger decrease in density when R_A decreases. This explains that σ_m^* decreases when R_A decreases. The characteristic wavelength λ_m^* decreases with $R_C - R_B$, and decreases with R_A, which is illustrated in Fig.9b.

5 Discussion

Figure 11 summarizes the classification of the effects of reactions in the parameter plane ($R_C - R_B$, R_A) by taking into account the analysis of the RD density profiles and the results of the LSA. When $R_C - R_B > 0$, the reactive density profile is more unstable than its non reactive counterpart if $R_A < \Delta_R$ (zone III). More specifically, if $R_A \leq 0$ (zone V), the reaction creates in the density profile a maximum at the origin of the buoyancy-driven instability. If $R_A > \Delta_R$ (zone II), the RD density profile is less unstable than its non reactive counterpart. Note that the numerical value of Δ_R might depend on the LSA technique used and on the criterium used for the classification (for example σ^* or t^0)

Table 1 Studies on reactive dissolution-driven instabilities

Zone	R_A	$R_C - R_B$	Case	References
I	> 0	< 0	Stabilizing	3
II	> 0	≥ 0 and $< \Delta_R$	Stabilizing	31–34
III	> 0	$> \Delta_R$	Destabilizing	13
IV	≤ 0	≤ 0	Stable	
V	≤ 0	> 0	Destabilizing	54

but the overall structure of profile classification is robust. When $R_C - R_B \leq 0$, the RD density profile remains stable like its non reactive counterpart if $R_A \leq 0$ (zone IV), and is less unstable than its non reactive counterpart if $R_A > 0$ (zone I).

The classification proposed in section 4 encompasses previous experimental or theoretical studies on reactive dissolution-driven instabilities (see Table 1). We first discuss the stabilizing cases observed in zone I and II. Budroni et al. [3] have shown that a reaction of an ester dissolving downwards into an aqueous solution of NaOH produced a density profile with a minimum ($R_C - R_B < 0$, zone I), so that the instability grows slower than in the non reactive case. We note that a similar stabilization by a minimum in the density profile has also been observed in an electrochemical system [53]. Other studies have shown that the reaction of the dissolving species CO_2 with a solid in excess, producing another solid, is expected to slow down the development of the dissolution-driven instability [31–34]. This type of reaction corresponds to the stabilizing case $R_A > 0$, $R_C = R_B = 0$ (zone II).

Destabilizing cases also exist in the literature. We have recently illustrated zone III ($R_A > 0$, $R_C - R_B > \Delta_R$) in an experimental study of gaseous CO_2 dissolving into a reactive aqueous solution of NaOH [13]. We have shown that the reaction between the dissolving CO_2 and the dissolved NaOH produces a chemical species sufficiently denser than the dissolved reactant, so that dissolution-driven convection develops faster than in the non reactive case [13]. The blue bottle reaction studied e.g. by Bees et al. [54] is an example of zone V ($R_A = 0$, $R_C > R_B = 0$) where the chemical reaction is at the origin of the buoyancy-driven instability. In their model, the reaction produces gluconic acid which increases the density of the solution, while the dissolving species and the dissolved reactants do not increase the density of the solution.

Although our study could be extended to take into account differences in diffusion coefficients [2,9] and/or to include different stoichiometries and reaction schemes [7,13,55], it can be used to predict behaviors in laboratory experiments. The values of the solutal Rayleigh number R_A, R_B and R_C tested here are relevant to laboratory experiments, for example in the case of CO_2 dissolving into an aqueous solution of NaOH, $R_A = 0.102$, $R_C - R_B = 0.760$ [13].

A realistic effect of reactions on dissolution-driven convection in underground storage sites for CO_2 sequestration is difficult to estimate because of the number of possible different reactions, feedback between chemistry and permeability/porosity, etc. We note that Ennis-King and Paterson [31] showed that the coupling of the concentrations of dissolved ions with the density of the solution affected the development of the dissolution-driven instability in a simulation of a realistic storage site. The fingers of denser fluid advanced faster in the system with the coupling than

Table 2 Typical values in geological storage sites for CO_2 sequestration[56]

Parameter	Symbol	Value
Porosity	ϕ	0.10
Permeability	κ	2×10^{-13} m^2
Viscosity	μ	10^{-3} Pa s
Diffusion coefficient of CO_2	D_A	5×10^{-9} m^2 s^{-1}
Density difference between CO_2 saturated brine and fresh brine	$\Delta\rho$	5 kg m^{-3}

without it, which indicated that the instability grew faster. With typical values in geological sites for CO_2 sequestration shown in Table 2, R_A can be of the order of 10^{-2} - 10^2 considering that the reaction rate can vary between 10^{-5} and 10^{-10} mol m^{-3} s^{-1} depending on the reaction[57]. Reactions in storage sites are often approximated as reactions between CO_2 and a solid to produce another solid. However, these reactions can also produce or consume dissolved salts. For example, the reaction of albite with CO_2 produces Na-smectite, silicon dioxide and sodium bicarbonate[33]. This reaction could possibly accelerate the dissolution-driven instability that develops upon dissolution of CO_2 in the saline aquifer ($R_A > 0$, $R_C > R_B = 0$).

6 Conclusion

We have proposed a general classification of the effects of reactions on the early-stage development of dissolution-driven convection, including cases where the non reactive counterpart is stable. This classification unifies previous disparate experimental and theoretical studies. It also sets the framework in which to predict the effects of reactions on dissolution-driven convection in natural and laboratory systems and to develop laboratory experiments to test our predictions. Further analysis of the impact of reactions on the late-stage nonlinear development of convection and on the evolution of the dissolution rate has been undertaken. We intend also to extend this classification to cases including differential diffusion and different stoichiometries[55]. Differential diffusion phenomena are indeed known to be able to impact the properties of convection or even be at the origin of double diffusive or diffusive layer convection instabilities in miscible systems[37,46]. It is expected that, similarly, the inclusion of differential diffusion in the present classification will enlarge the number of possible different instability scenarios.

In the context of CO_2 sequestration, such classifications allow comparing different geological storage sites according to their dominant mineralogy and select those where reactions are optimal in enhancing convective dissolution. For other applications where convection enhances mass transfer, controlling the properties of the dissolution-driven convection should become possible by selecting the appropriate reactant to be dissolved in the host solution.

Acknowledgments

We thank P.M.J. Trevelyan and M.A. Budroni for fruitful discussions. V.L. is F.R.S.-FNRS Research Fellow. Funding by Prodex, ARC CONVINCE and PDR-FNRS FORECAST projects is gratefully acknowledged.

References

1 D. Avnir and M. Kagan, Nature, 1984, **307**, 717–720.
2 O. Citri, M. L. Kagan, R. Kosloff and D. Avnir, Langmuir, 1990, **6**, 559–564.
3 M. A. Budroni, L. A. Riolfo, L. Lemaigre, F. Rossi, M. Rustici and A. De Wit, J. Phys. Chem. Lett., 2014, **5**, 875–881.
4 M. Lappa, C. Piccolo and L. Carotenuto, Colloids Surf. A, 2005, **261**, 177–186.
5 A. C. Slim, M. M. Bandi, J. C. Miller and L. Mahadevan, Phys. Fluids, 2013, **25**, 024101.
6 C. Wylock, S. Dehaeck, A. Rednikov and P. Colinet, Microgravity Sci. Tec., 2008, **20**, 171–175.
7 C. Wylock, S. Dehaeck, T. Cartage, P. Colinet and B. Haut, Chem. Eng. Sci., 2011, **66**, 3400–3412.
8 C. Wylock, S. Dehaeck, D. Alonso Quintans, P. Colinet and B. Haut, Chem. Eng. Sci., 2013, **100**, 249–258.
9 C. Wylock, A. Rednikov, B. Haut and P. Colinet, J. Phys. Chem. B, 2014, **118**, 11323–11329.
10 T. J. Kneafsey and K. Pruess, Transp. Porous Med., 2010, **82**, 123–139.
11 T. J. Kneafsey and K. Pruess, Energy Procedia, 2011, **4**, 5114–5121.
12 R. Outeda, A. Zalts, C. El Hasi and A. D'Onofrio, Chaos, 2014, **24**, 013135.
13 V. Loodts, C. Thomas, L. Rongy and A. De Wit, Phys. Rev. Lett., 2014, **113**, 114501.
14 A. Firoozabadi and P. Cheng, AIChE J., 2010, **56**, 1398–1405.
15 H. E. Huppert and J. A. Neufeld, Annu. Rev. Fluid Mech., 2014, **46**, 255–272.
16 J. Ennis-King and L. Paterson, SPE J., 2005, **10**, 349–356.
17 L. Rongy, K. B. Haugen and A. Firoozabadi, AIChE J., 2012, **58**, 1336–1345.
18 A. Riaz, M. Hesse, H. A. Tchelepi and F. M. Orr, J. Fluid Mech., 2006, **548**, 87–111.
19 V. Loodts, L. Rongy and A. De Wit, Chaos, 2014, **24**, 043120.
20 D. A. S. Rees, A. Selim and J. P. Ennis-King, Emerging Topics in Heat and Mass Transfer in Porous Media, Springer Netherlands, 2008, pp. 85–110.
21 H. Hassanzadeh, M. Pooladi-Darvish and D. W. Keith, Transp. Porous Med., 2006, **65**, 193–211.
22 A. C. Slim and T. S. Ramakrishnan, Phys. Fluids, 2010, **22**, 124103.
23 J. Ennis-King, I. Preston and L. Paterson, Phys. Fluids, 2005, **17**, 084107.
24 X. Xu, S. Chen and D. Zhang, Adv. Water Res., 2006, **29**, 397–407.
25 P. Cheng, M. Bestehorn and A. Firoozabadi, Water Resour. Res., 2012, **48**, W09539.
26 P. C. Myint and A. Firoozabadi, Phys. Fluids, 2013, **25**, 044105.
27 P. C. Myint and A. Firoozabadi, Phys. Fluids, 2013, **25**, 094105.

28 M. Bestehorn and A. Firoozabadi, Phys. Fluids, 2012, **24**, 114102.
29 M. Javaheri, J. Abedi and H. Hassanzadeh, Transp. Porous Med., 2010, **84**, 441–456.
30 Y.-S. Jun, D. E. Giammar and C. J. Werth, Environ. Sci. Technol., 2013, **47**, 3–8.
31 J. Ennis-King and L. Paterson, Int. J. Greenh. Gas Con., 2007, **1**, 86–93.
32 J. T. H. Andres and S. S. S. Cardoso, Phys. Rev. E, 2011, **83**, 046312.
33 K. Ghesmat, H. Hassanzadeh and J. Abedi, J. Fluid Mech., 2011, **673**, 480–512.
34 T. Ward, K. Cliffe, O. Jensen and H. Power, J. Fluid Mech., 2014, **747**, 316–349.
35 C. Almarcha, P. M. J. Trevelyan, P. Grosfils and A. De Wit, Phys. Rev. Lett., 2010, **104**, 044501.
36 A. De Wit, Phys. Rev. Lett., 2001, **87**, 054502.
37 L. Lemaigre, M. A. Budroni, L. A. Riolfo, P. Grosfils and A. De Wit, Phys. Fluids, 2013, **25**, 014103.
38 K. Eckert and A. Grahn, Phys. Rev. Lett., 1999, **82**, 4436.
39 L. Rongy, P. M. J. Trevelyan and A. De Wit, Phys. Rev. Lett., 2008, **101**, 084503.
40 L. Rongy, P. Trevelyan and A. De Wit, Chem. Eng. Sci., 2010, **65**, 2382–2391.
41 C. Almarcha, P. M. J. Trevelyan, P. Grosfils and A. De Wit, Physical Review E, 2013, **88**, 033009.
42 J. J. Hidalgo and J. Carrera, J. Fluid Mech., 2009, **640**, 441.
43 E. Guyon, J.-P. Hulin, L. Petit and C. Mitescu, Physical Hydrodynamics, Oxford University Press, 2001.
44 M. T. Elenius and K. Johannsen, Comput. Geosci., 2012, **16**, 901–911.
45 L. Gálfi and Z. Rácz, Phys. Rev. A, 1988, **38**, 3151.
46 P. M. J. Trevelyan, C. Almarcha and A. De Wit, Phys. Rev. E, 2015, **91**, 023001.
47 J. D. Faires and R. Burden, Numerical Methods, Brooks/Cole, Cengage Learning, 4th edn, 2013.
48 N. Tilton, D. Daniel and A. Riaz, Phys. Fluids, 2013, **25**, 092107.
49 M. Chan Kim and C. Kyun Choi, Phys. Fluids, 2012, **24**, 044102.
50 S. Kalliadasis, J. Yang and A. De Wit, Phys. Fluids, 2004, **16**, 1395–1409.
51 P. M. J. Trevelyan, C. Almarcha and A. De Wit, J. Fluid Mech., 2011, **670**, 38–65.
52 A. C. Slim, J. Fluid Mech., 2014, **741**, 461–491.
53 S. Mühlenhoff, K. Eckert, A. Heinze and M. Uhlemann, J. Electroanal. Chem., 2007, **611**, 241–249.
54 M. A. Bees, A. J. Pons, P. G. Sørensen and F. Sagués, J. Chem. Phys., 2001, **114**, 1932.
55 P. Trevelyan, Phys. Rev. E, 2009, **79**, 016105.
56 H. Hassanzadeh, M. Pooladi-Darvish and D. W. Keith, AIChE J., 2007, **53**, 1121–1131.
57 J. W. Johnson, J. J. Nitao and K. G. Knauss, Geol. Soc. London Spec. Publ., 2004, **233**, 107–128.